

Enhanced Light Absorption and Radiative Forcing by Black Carbon Agglomerates

Georgios A. Kelesidis,* David Neubauer, Liang-Shih Fan, Ulrike Lohmann, and Sotiris E. Pratsinis



Cite This: *Environ. Sci. Technol.* 2022, 56, 8610–8618



Read Online

ACCESS |



Metrics & More



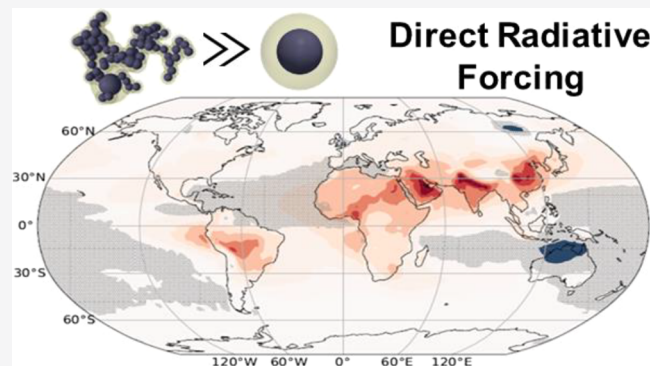
Article Recommendations



Supporting Information

ABSTRACT: The climate models of the Intergovernmental Panel on Climate Change list black carbon (BC) as an important contributor to global warming based on its radiative forcing (RF) impact. Examining closely these models, it becomes apparent that they might underpredict significantly the direct RF for BC, largely due to their assumed spherical BC morphology. Specifically, the light absorption and direct RF of BC agglomerates are enhanced by light scattering between their constituent primary particles as determined by the Rayleigh–Debye–Gans theory interfaced with discrete dipole approximation and recent relations for the refractive index and lensing effect. The light absorption of BC is enhanced by about 20% by the multiple light scattering between BC primary particles regardless of the compactness of their agglomerates. The resulting light absorption agrees very well with the observed absorption aerosol optical depth of BC. ECHAM-HAM simulations accounting for the realistic BC morphology and its coatings reveal high direct RF = 3–5 W/m² in East, South Asia, sub-Sahara, western Africa, and the Arabian peninsula. These results are in agreement with satellite and AERONET observations of RF and indicate a regional climate warming contribution by 0.75–1.25 °C, solely due to BC emissions.

KEYWORDS: black carbon, morphology, optical properties, mass absorption cross-section, radiative forcing



1. INTRODUCTION

Incomplete combustion of fossil or biofuels and open fires release about 8 Tg of black carbon (BC) per year worldwide.¹ This is on the same order of magnitude as the global annual production of carbon black (11 Tg).² BC (also known as mature soot) is made of porous, fractal-like clusters (agglomerates) of nanoparticles³ that are coated with weakly or non-absorbing compounds (e.g., organics, sulfates, ammonium, nitrates, and water) during atmospheric aging.⁴ Unlike CO₂ that has an atmospheric lifetime of 200–1000 years depending on CO₂ removal processes,⁵ BC is a short-lived pollutant with a lifetime of about 4–7 days.⁶ Therefore, reducing BC emissions can have an immediate impact on global warming⁷ and delay climate change⁸ induced by CO₂ and other greenhouse gases.

Light absorption and scattering of BC yield together its direct RF, which is used to quantify its climate impact⁹ and to estimate its 100-year global warming potential.¹⁰ The direct RF depends on BC atmospheric burden, absorption forcing efficiency, refractive index, *RI*, and mass absorption cross-section, *MAC*¹. The latter is the light absorption-equivalent cross-section of BC normalized by its mass and varies significantly with BC composition and morphology.³ At the top of the atmosphere (TOA), the climate may warm by 0.25

± 0.21 °C for every watt per square meter (W/m²) of Earth's surface of BC's direct RF¹¹. Interactions of BC with snow¹² and clouds¹³ are reported by Intergovernmental Panel on Climate Change (IPCC) as a separate global warming contribution and may indirectly increase the BC RF. In fact, recent global climate simulations revealed that BC may indirectly increase the global mean surface temperature by 0.4–0.5 °C through its interactions with clouds.¹³ In contrast, rapid adjustments, such as the warming of the troposphere and the reduction of low clouds, could reduce the effective RF from BC.¹⁴

The contribution of BC to climate change is estimated with the highest uncertainty (~90%)¹ in climate models, limiting their accuracy.¹⁵ Specifically, climate models of the 2021 IPCC report¹⁶ estimate BC's RF to range from –0.28 to 0.41 W/m², increasing the globally averaged TOA temperature up to 0.1 °C in 1750–2019. This large uncertainty can be attributed, next to the uncertainty in BC emissions and lifetime, to BC

Received: January 19, 2022

Revised: May 17, 2022

Accepted: May 19, 2022

Published: June 2, 2022



morphology and composition variations that are neglected by climate models.¹⁷ Therefore, the direct *RF* range in 1750–2011 derived by IPCC models for BC spheres with unrealistic *RI* (as shown below) is 30% smaller than that obtained based on satellite¹⁸ and ground-based¹⁹ (AERONET) observations by Bond et al.¹ and Chung et al.,²⁰ respectively. Accounting for the coating of BC spheres increased the direct *RF* but only partly reduced the discrepancy between observations and climate models²¹ as the latter still neglect the ramified BC morphology. Even though concern about such oversimplifications of BC morphology and *RI* had been expressed since, at least, 30 years ago,²² they are still used today in climate models.

To account for the morphology and *RI* of BC in determination of its direct *RF*, the Rayleigh–Debye–Gans (RDG) theory²³ can be used as a more flexible alternative to Mie theory in climate models. This way, recent power laws relating the optical properties of BC to its filamentary structure based on discrete element modeling (DEM)²⁴ and discrete dipole approximation (DDA)²⁵ can be implemented in such models. These laws have been used quite effectively to describe BC formation and growth from a variety of combustion sources²⁴ and even facilitate monitoring of BC emissions by aerosol (e.g., particle mobility and mass analyzers), laser (e.g., light extinction) diagnostics,²⁶ and fire detectors²⁷ accounting for BC morphology and limiting the current uncertainty regarding BC mass and particle size.²⁸ This way, the light absorption and scattering of BC can be estimated quite accurately even though BC is made up of coated polydisperse and fused nanoparticles. Here, the RDG theory is interfaced with DDA simulations (open-source DDSCAT 7.3 code) and recent relations for the *RI*²⁵ and lensing effect²⁹ of BC to estimate its light absorption and scattering accounting for its morphology and coating by weakly or non-absorbing compounds. The *MAC* and the global and regional climate impact of emissions of coated BC with realistic morphology and *RI* are estimated by the RDG theory used in simulations with the global climate model ECHAM-HAM and compared to that impact by coated mass-equivalent BC spheres that are widely used by climate models.

2. MATERIALS AND METHODS

2.1. BC Optical Properties. The *MAC* is estimated for BC agglomerates using the RDG theory:^{23,30}

$$MAC = h \frac{6\pi}{\lambda \cdot \rho} \text{Im} \left(\frac{RI^2 - 1}{RI^2 + 2} \right) \quad (1)$$

where $\rho = 1.8 \text{ g/cm}^3$ and $RI = 1.66 - 0.76i$ are the bulk density and refractive index (at wavelength, $\lambda = 532 \text{ nm}$), respectively, of C-rich BC, while h is the *MAC* enhancement by the multiple light scattering of the constituent primary particles of BC agglomerates. Eq 1 with $h = 1$ neglects any absorption enhancement by this multiple internal scattering making it the *MAC* of mass-equivalent BC spheres. Here, h (Supporting Information, Figure S1, squares) is derived using DEM coupled with DDA.²⁵ Unlike the T-matrix method used for agglomerates of physically bonded (non-overlapping) primary particles,³¹ DDA can be used to derive the light absorption and multiple light scattering from both physically and chemically bonded BC primary particles.²⁵

In brief, BC spheres and agglomerates of polydisperse and chemically bonded (aggregated) primary particles with

mobility diameter, $d_m = 50\text{--}250 \text{ nm}$ and $d_p = 7.5\text{--}40 \text{ nm}$, are generated by DEM for BC surface growth and agglomeration.²⁴ This d_p range covers the variation of soot d_p measured from engines and laboratory flames as summarized by Bond and Bergstrom³ (Figure 1: shaded red

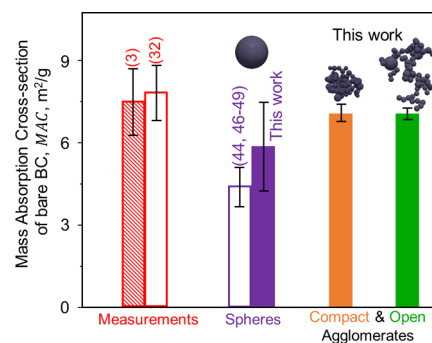


Figure 1. Bare BC *MAC* calculated at $\lambda = 550 \text{ nm}$ for spheres (filled purple bar), compact (orange bar), and open agglomerates (green bar) as well as the average *MAC* from 11 climate models^{44,46–49} for bare spheres (open purple bar). The *MAC* of open and compact agglomerates are in agreement with those measured for soot from diesel engines and flame reactors and averaged over 17 studies from 1967 to 2005 by Bond and Bergstrom³ (shaded red bar) and over 24 studies from 2002 to 2018 by Liu et al.³² (open red bar).

bar) and Liu et al.³² (Figure 1: open red bar). The morphology of these open agglomerates having a fractal dimension, D_f , of about 1.91 has been validated with microscopy,³³ mass-mobility,²⁴ and light scattering²⁷ measurements of diffusion and pre-mixed flame soot. Compact agglomerates of polydisperse primary particles in point contact having the same d_p and $\sigma_{g,p}$ with the open agglomerates are generated³⁴ using the open source FracVal algorithm.³⁵ The compact BC agglomerates simulated here³⁴ have $D_f = 2.76$. Their d_m is nearly equal (within 2%) to their gyration diameter (Figure 3b in ref 36) and results in a mass-mobility exponent, $D_{fm} = 2.65 \pm 0.01$. This is in good agreement with the D_{fm} values from the analysis³⁷ of mass-mobility measurements of BC agglomerates produced by pre-mixed, diffusion flames and diesel soot generators and compacted by condensation and evaporation of secondary organic aerosols ($D_f = 2.64\text{--}2.73$).³⁸ The DDA computations are then performed using the open-source DDSCAT 7.3 code³⁹ for each d_m . The particle morphology is represented on a lattice by an array of discrete dipoles interacting with each other through their electric fields.³⁹ The Maxwell's equations are discretized on the lattice using the volume-integral equation method and solved iteratively.³⁹ For accurate but also efficient DDA computations, the dipole spacing, d , is varied at a constant ratio $2\pi|RI|d/\lambda < 0.12$, satisfying the precision criteria⁴⁰ for strongly absorbing materials, such as BC.

The DDA-derived optical properties of spheres are identical to those estimated by Mie theory (Figure S1 in ref 27). Therefore, h is estimated from the ratio of the DDA-derived *MAC* over that given by the classic RDG theory (eq 1 with $h = 1$)³⁰ for BC agglomerates of polydisperse single and aggregated primary particles with $d_m = 50\text{--}250 \text{ nm}$ and $d_p = 7.5\text{--}40 \text{ nm}$ at $\lambda = 532 \text{ nm}$ (Figure S1, squares). For $d_m > 50 \text{ nm}$, BC agglomerates have C-rich composition ($C/H > 4$) and a ramified morphology.²⁵ Therefore, their h attains its asymptotic value of 1.18 ± 0.03 (Figure S1, broken line and

green-shaded area). This is in agreement with the h derived from DDA simulations of agglomerates with monodisperse, single primary particles (triangles).³⁰ The enhancement of the light absorption from compact BC agglomerates (circles) is similar to that from open ones with polydisperse and aggregated (squares) and monodisperse (triangles) primary particles, resulting in an average $h = 1.17 \pm 0.04$ (dot-broken line, orange-shaded area). Therefore, the BC h is not affected by the agglomerate compactness or primary particle polydispersity and aggregation.

The MAC of bare BC spheres and agglomerates derived here at $\lambda = 532$ nm are interfaced with an absorption Angstrom exponent of 1.1 to estimate their MAC at $\lambda = 550$ nm accounting for the wavelength dependence of C-rich BC.⁴¹ Furthermore, the MAC_c of coated BC is estimated directly from the MAC of emitted BC by a scaling law from DDA simulations:²⁹

$$MAC_c = MAC \cdot (m_c/m)^{0.32 \pm 0.05} \quad (2)$$

where m and m_c are the mass of BC before and after coating with non-absorbing compounds, respectively. Therefore, m_c includes the mass of both BC and coating species. Unlike the RDG theory, the DDA is not limited by the d_p or d_m range.³⁹ Therefore, eq 2 can be used to estimate the BC light absorption for m_c/m even up to 50. Eq 2 was validated with laboratory cook stove,⁴² biomass, diesel generator, ambient traffic,⁴³ and field²¹ data. The ease or difficulty of BC encapsulation by coatings is not accounted here.

2.2. Absorption Aerosol Optical Depth of BC. The global mean absorption aerosol optical depth, AAOD, of BC is estimated using the BC MAC and average atmospheric burden, N^1 :

$$AAOD = N \cdot MAC \quad (3)$$

where $N = 0.29 \pm 0.11$ mg/m² is obtained based on those reported by recent climate models using lifetimes of 2.2–9.6 days⁴⁴ (Table S1). This lifetime range is on par with the lifetimes used for hydrophobic and hydrophilic BC⁴⁵. The AAOD of BC is obtained using eq 3 with the MAC derived here for bare and coated spheres and agglomerates, as well as the average MAC used in climate models for bare^{44,46–49} (Table S2) and coated⁴⁴ (Table S1) spheres. The BC AAOD estimated this way is compared to that obtained based on ground-based AERONET observations⁵⁰ of the total AAOD, as well as to the average contribution of BC to the total AAOD derived by recent climate models⁴⁴ of the AeroCom phase III. These models have been used in the 6th assessment report (AR6) of the IPCC to obtain the direct RF of BC for the period of 1750–2019.¹⁶

The uncertainty of AAOD from BC, σ_{AAOD} , derived by eq 3 is given by propagation theory, assuming that the BC N and MAC are independent:⁵¹

$$\sigma_{AAOD} = \sqrt{(\sigma_{MAC}N)^2 + (MAC \cdot \sigma_N)^2} \quad (4)$$

where $\sigma_N = 0.11$ mg/m² and σ_{MAC} are the uncertainties of N and MAC, respectively. The σ_N is estimated from the standard deviation of 15 climate models⁴⁴ (Table S1). The σ_{MAC} for bare BC agglomerates is based on the standard deviation of h (Figure S1). The σ_{MAC} for coated BC particles accounts also for the standard deviation of the average m_c derived by detailed climate modeling.⁴ It should be noted that the BC emission rate, E , and lifetime, τ , vary also significantly between different

climate models, resulting in the large $\sigma_N = 0.11$ mg/m² (about 40%; Table S1). Unlike E and τ though, the BC MAC can be determined from first principles based on recent computational advances, reducing the total uncertainty of soot's climate impact estimation bringing its contribution to RF very close to the 2001–2009 satellite record and 2010 AERONET data (Figure 3 or 4).

2.3. Regional Direct RF by ECHAM-HAM Simulations.

The global direct RF distributions of bare or coated BC spheres and agglomerates RF in the industrial era are obtained based on the difference of the BC direct radiative effect between 1850 and 2010 using the global coupled aerosol-climate model ECHAM-HAM in T63 spectral horizontal resolution, which corresponds to a regular $1.875^\circ \times 1.875^\circ$ grid. The model has 31 vertical levels with a top at 10 hPa and uses a time step of 7.5 min¹³. All simulations are performed with the prescribed climatological sea surface temperature and sea ice extents representative for the years 2000–2015 and aerosol emissions representative for 2010 using CMIP6 aerosol emission data. The setup of the simulations presented here closely follows the one in Neubauer et al.⁵² The quantification of the direct BC RF follows the protocol in Myhre et al.⁵³ The ECHAM-HAM simulations also account for particles that do not contain BC, including dust, sea salt, sulfates, and organics. Therefore, BC-containing particles make up 0.5 wt % of the total particles (fine and coarse and 5% of the fine alone) in the model.⁵⁴ Aging of externally mixed BC and mineral dust aerosols is considered by condensation of sulfuric acid and coagulation of bare BC and/or dust particles with internally mixed aerosols that contain soluble materials and converts them into internally mixed particles.¹³ Eq 2 is interfaced with the mass concentrations of BC, sulfates, and organics derived by ECHAM-HAM to obtain the spatial (Figure S2) and the vertical distribution of m_c/m (Figure S3: dotted line). In this regard, as the pressure, p , decreases with altitude, m_c/m increases from 11 up to 46 from the surface to the tropopause, consistent with the large mass-to-core ratios of 50 measured by Ditas et al.⁵⁵ The increasing m_c/m estimated here for decreasing p is consistent with the high coatings measured above the clouds over urban Eastern China.⁵⁶ This results also in an up to 400% increase of absorption forcing efficiency with decreasing p (Figure S3: solid line), consistent with previous climate model studies.⁵⁷ The BC optical properties are accounted for in ECHAM-HAM simulations using the MAC derived at $\lambda = 532$ nm for bare or coated BC spheres and agglomerates and the DDA-derived absorption Angstrom exponent of 1.1 to account for the wavelength dependence of C-rich BC light absorption.⁴¹ The global and regional direct RF from BC is compared to satellite¹⁸ and ground-based AERONET observations,¹⁹ respectively, by interfacing the measured BC AAOD with the absorption wavelength dependence of BC, dust, and organic matter,²⁰ as well as with GOCART²⁰ and CAMS¹ climate models.

3. RESULTS AND DISCUSSION

3.1. Light Absorption by Bare and Coated BC. Bare BC emitted from combustion engines or open flames is rather filamentary with large C/H ratio (>4), bulk density, $\rho = 1.8$ g/cm³, and $RI = 1.66–0.76i$.²⁵ However, climate models^{44,46–49} estimate BC light absorption assuming spheres with small imaginary RI parts (Table S2) that are similar to those of H-rich BC (young soot)-containing organic carbon formed at short residence times.⁴¹ Such unrealistic BC RI values are still

used in almost half of the most recent climate models⁴⁴ included in the IPCC AR6 (Table S1). These RI combined with $\rho = 1.8 \text{ g/cm}^3$ result in BC $MAC = 4.4 \pm 0.7 \text{ m}^2/\text{g}$ (Figure 1: open purple bar). The bare BC MAC values from the IPCC AR6 models⁴⁴ are almost identical to those^{46–49} used in the IPCC AR5 (Table S2). The average BC MAC from these climate models^{44,46–49} is about 40% smaller than the MAC measured in diesel engines and laboratory flames averaged over 17 studies from 1967 to 2005 by Bond and Bergstrom³ and over 24 studies from 2002 to 2018 by Liu et al.³² The $MAC = 5.9 \pm 1.6 \text{ m}^2/\text{g}$ (filled purple bar) derived here by DDA for C-rich (equivalent to BC) spheres with $RI = 1.66–0.76i$ still underestimates the measured MAC (red bars) by 21–24%. This underestimation is due to the porous structure of BC agglomerates that enhances the light scattering and subsequent absorption in between their constituent primary particles by up to 18% (Figure S1).

The original RDG theory (eq 1 with $h = 1$) does not account for the multiple light scattering between BC primary particles in their agglomerates.²³ This underestimates the MAC of BC by about 15–21% (Figure S1: $h = 1.15–1.21$) and results in identical light absorption to that obtained for spheres ($6 \text{ m}^2/\text{g}$, Figure 1: filled purple bar). In contrast, a MAC of $7.1 \pm 0.2 \text{ m}^2/\text{g}$ (Figure 1: filled green bar) is obtained for BC agglomerates by the RDG theory (eq 1) using the DDA-derived $h = 1.18 \pm 0.03$. This MAC accounts for the interactions between BC primary particles and agrees with soot measurements from laboratory flames and diesel engines (Figure 1: shaded³ and open³² red bars). The MAC of compact BC agglomerates (orange bar) is identical to that obtained from open ones (green bar). This is consistent with MAC measurements of ramified and compact BC⁵⁸ from a diffusion flame and confirms that the light absorption of BC is enhanced by the multiple light scattering between BC primary particles regardless of the compactness of their agglomerates. This enhancement is not accounted for by models neglecting the ramified structure of BC.

During atmospheric aging, BC is coated by weakly or non-absorbing compounds, such as organics, sulfates, ammonium, nitrates, and water.⁴ These non-absorbing compounds have an average refractive index,²⁹ RI_c of 1.55 ± 0.32 and a density, ρ_c of $1.2 \pm 0.2 \text{ g/cm}^3$. The standard deviations of RI_c and ρ_c account for their variation with light wavelength and coating composition.⁵⁹ These coatings enhance BC light absorption based on a DDA-derived power law²⁹ that relates the coated BC mass, m_c , and MAC_c to the bare BC m and MAC (eq 2). The impact of the RI_c variation with wavelength or composition (e.g., due to photobleaching) on the MAC enhancement is rather negligible.²⁹ Photobleaching may reduce the imaginary part⁶⁰ of RI_c from 0.1 to 0.

BC agglomerates have larger surface areas than non-BC-containing aerosol spheres due to their ramified structure.³³ This may enhance the volatile condensation on the BC surface by up to a factor of 3⁶¹ and explains the difference in the BC-coating composition compared to that in non-BC-containing particles. According to particle-resolved models that account for the spatial variation of BC composition,⁴ BC coatings consist on average of 32 vol % of primary and secondary organic aerosols, 5.5% of sulfates, 16% of ammonium, and 46.5% of nitrates. It should be noted that the above-quoted BC-coating composition is the global average. The regional BC-coating composition can vary based on the local aerosol concentrations. For example, nitrate concentrations are high

mostly in the urban atmosphere of North America, Europe, India, and East China and rather low in remote regions.⁶² The average mass fraction of 5.5% used here to account for sulfates in the BC coating is on par with such measurements in China (2.5–10.5% by Wang et al.⁶³ Figures 2, 6, and 7) and US (1% by Collier et al.⁶⁴ Figure 5). Similarly, the mass fraction of 46.5% used here for nitrate coating on BC is on par with the 30–40% nitrate mass fraction measured in the UK (McMeeking et al.⁶⁵ Figure 5), as well as with the 40% number-based fraction of nitrate-containing BC measured in China (Gong et al.⁶⁶ Table 1). These coatings have, on average, about a 7 times larger volume than the BC core.⁴ Assuming densities $\rho = 1.8 \text{ g/cm}^3$ and $\rho_c = 1.2 \pm 0.2 \text{ g/cm}^3$ for the BC and its coatings,²⁹ respectively, results in $m_c/m = 5.6 \pm 0.8$ (Figure S4). The standard deviation of m_c/m was derived accounting for the variation of ρ_c with the coating composition. The $m_c/m = 5.6 \pm 0.8$ estimated here is on par with the $m_c/m = 1.7–9.9$ measured over the North China Plain during different seasons.⁶⁷ This m_c/m results in $MAC_c = 10.2 \pm 4.1$ and $12.3 \pm 1.2 \text{ m}^2/\text{g}$ for spheres and agglomerates, respectively. The former is in excellent agreement with the average $MAC_c = 9.8 \pm 4.1 \text{ m}^2/\text{g}$ obtained by recent climate models⁴⁴ assuming coated BC spheres (Table S1). Compacting of BC agglomerates entities by vapor condensation during aging hardly (within 5%) affects their MAC ⁵⁸ (as shown also in Figure 1: orange vs green bar). Therefore, the MAC_c of coated ramified agglomerates is assumed to be the same as that of coated restructured ones.

The MAC_c of coated BC was also obtained for a wide range of $m_c/m = 1–10$ and compared to cook stove data⁴² (Figure 2). The $MAC_c = 9.2 \pm 1.5 \text{ m}^2/\text{g}$ obtained at $m_c/m = 10$ by

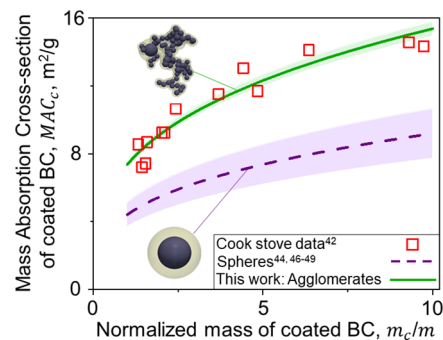


Figure 2. MAC_c of coated BC as a function of its normalized mass, m_c/m , derived here for agglomerates (solid line) and by IPCC models^{44,46–49} for spheres (broken line) in comparison to cook stove data (symbols).⁴² Variation of MAC_c due to the initial MAC of uncoated spheres and agglomerates is represented by the shaded area. The MAC_c obtained for coated BC spheres by IPCC models (broken line) underestimates the measured MAC_c (symbols) by 25–40%. In contrast, the MAC_c of coated BC agglomerates (solid line) is in excellent agreement with the data for the whole range of m_c/m .

interfacing eq 2 with the average bare BC $MAC = 4.4 \pm 0.7 \text{ m}^2/\text{g}$ from IPCC AR5 and AR6 models^{44,46–49} is in excellent agreement with the average $MAC_c = 9.8 \pm 4.1 \text{ m}^2/\text{g}$ used in the IPCC AR6 models⁴⁴ (Table S1). The MAC_c obtained for coated BC spheres by IPCC models^{44,46–49} (broken line) underestimates the measured MAC_c (symbols) by 25–40%. In contrast, the MAC_c of coated BC agglomerates (solid line) is in excellent agreement with the data for the whole range of m_c/m . Furthermore, the $MAC_c = 12.3 \pm 1.2 \text{ m}^2/\text{g}$ derived here for

coated BC agglomerates having the average coating composition is in good agreement with the mode $MAC_c = 12.7 \pm 0.1 \text{ m}^2/\text{g}$ measured before, during, and after daytime photochemical oxidation in China.⁶⁸ This indicates that the MAC_c derived here accounting for the realistic BC morphology and coating may provide more accurate estimates of the direct RF from BC than those given in the wider literature.

Even though the main focus of this paper is the accurate estimation of the BC light absorption and MAC , it should be noted that the BC agglomerate structure and coating also affect its light scattering and phase parameters that are essential for climate modeling. For example, the BC single scattering albedo, SSA , is given by the ratio of the BC external light scattering over its light extinction¹ and increases with increasing m_c/m (Figure S5a). This is due to the enhanced light scattering by the BC coating.⁴¹ The SSA of BC agglomerates (solid line, light green-shaded area) is smaller than that of equivalent spheres (broken line, purple-shaded area) at $m_c/m = 1-10$. This is attributed to the internal light scattering between the constituent primary particles of agglomerates that increases their light absorption (Figure S1) but reduces their external light scattering.

The BC asymmetry factor, g , quantifies the asymmetry of its angular light scattering distribution and is given by its phase parameters.¹ The light scattering of BC agglomerates is rather asymmetric as it decreases logarithmically with increasing scattering angle.²⁷ This results in a rather constant g of about 0.84 regardless of m_c/m (Figure S5b: solid line, light green-shaded area). In contrast, the light scattering distribution of uncoated BC spheres (broken line, purple-shaded area: $m_c/m = 1$) is rather uniform, resulting in $g = 0.19$. As m_c/m increases and the BC spheres become larger due to their coating, their g increases up to 0.84 at $m_c/m = 10$, in good agreement with the g of coated BC agglomerates having the same coating amount.

3.2. Climate Change Contribution by BC. The good agreement of the MAC from RDG theory with measurements (Figure 1: green vs red bars) supports its use to estimate the global and regional climate impact of BC. The BC climate impact estimated here is benchmarked to that derived by recent climate models for bare and coated BC spheres. Therefore, Figure 3 shows the BC $AAOD$ estimated here by

multiplying the average $N = 0.29 \pm 0.11 \text{ mg}/\text{m}^2$ obtained by recent climate models using the CMIP6 emission data (Table S1) with $MAC = 10.2 \pm 4.1 \text{ m}^2/\text{g}$ and $5.9 \pm 1.6 \text{ m}^2/\text{g}$ for BC spheres with (filled red bar) and without (filled purple bar) coatings, respectively, and $MAC = 12.3 \pm 1 \text{ m}^2/\text{g}$ and $7.1 \pm 0.2 \text{ m}^2/\text{g}$ for BC agglomerates with (blue bar) and without (green bar) coatings, respectively. Based on the climate models included in the IPCC AR6 (Figure 3 in ref 44), the BC $AAOD$ is concentrated mostly over land and is negligible in remote regions (e.g., over oceans). Therefore, the estimated BC $AAOD$ can be compared consistently with that from the AERONET network^{44,50} observation sites that are located over land. The latter has been the main standard so far to assess the accuracy of climate models.⁶⁹ The BC $AAOD_s = 0.0017 \pm 0.007$ and 0.003 ± 0.0016 obtained here for bare and coated spheres, respectively, are in excellent agreement with those obtained by climate models for bare^{44,46-49} (open purple bar) and coated spheres⁴⁴ (open red bar) using the same average N . The good agreement between the $AAOD$ estimated here for bare (Figure 3: filled purple bar) and coated (filled red bar) spheres with those estimated by climate models (open purple^{44,46-49} and red⁴⁴ bars) evaluated at the same conditions validates our numerical methods for the estimation of BC optical properties and direct RF . Accounting for the ramified BC morphology increases the $AAOD$ of bare and coated BC up to 0.0021 ± 0.0008 and 0.0036 ± 0.0014 , respectively. Therefore, the $AAOD$ derived here for coated BC agglomerates is about 30% larger than that obtained by the most recent climate models for coated spheres and is in good agreement with that observed by the AERONET network^{44,50} (yellow bar). A global mean direct $RF = 0.61 \pm 0.28 \text{ W}/\text{m}^2$ from coated BC agglomerates can be obtained by multiplying their $AAOD = 0.0036 \pm 0.0014$ with the average absorption forcing efficiency of $170 \pm 43 \text{ W}/\text{m}^2/\text{AAOD}$ used in global climate models.¹ This direct RF is in excellent agreement with the $0.65 \pm 0.15 \text{ W}/\text{m}^2$ from satellite measurements²⁰ between 2001 and 2009 (Figure S6). It should be noted that the enhancement of the BC $AAOD$ and global mean direct RF due to its agglomerate structure is also valid for the 1750–2019 RF estimates reported in the latest IPCC AR6 using the most recent climate models⁴⁴ of the AeroCom phase III (Table S1).

The global mean $AAOD$ of BC (Figure 3) affects primarily the climate of regions with high BC emissions, such as East and South Asia, the sub-Sahara, western Africa, South America, and the Arabian peninsula.⁷⁰ This is elucidated in the global maps of direct RF (Figure 4) obtained using ECHAM-HAM⁵² simulations for coated BC spheres (a) and agglomerates (b), respectively. The distribution of direct RF depends on the spatial variations of m_c/m (Figure S2). The latter is obtained by interfacing eq 2 with the mass concentrations of BC, sulfates, and organics derived by ECHAM-HAM. The spatial distribution of m_c/m is identical for coated spheres and agglomerates. The m_c/m derived here (Figure S2) ranges from 5 to 25 in regions where the BC direct RF is statistically significant. This is on par with m_c/m observations that range from 1.7⁶⁷ to 50.⁵⁵ Over the Pacific and Atlantic oceans, as well as over Australia, BC is coated by large amounts of sulfates and organics increasing m_c/m up to 35 (Figure S2). However, the direct RF induced by such heavily coated BC in these regions is statistically not significant (Figure 4: blue and dotted regions) due to its low mass concentrations and lifetime.⁴⁵ In contrast, the m_c/m of BC emissions over the North and South Poles ranges from 0 to 10 but results in a small, positive direct RF of

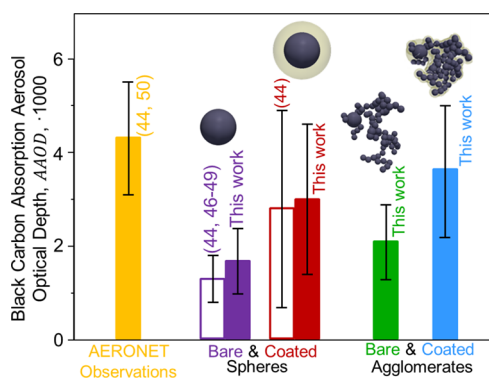


Figure 3. BC absorption aerosol optical depth ($AAOD$) estimated here for BC spheres with (filled red bar) and without coatings (filled purple bar), as well as for bare (green bar) and coated (blue bar) BC agglomerates compared to those obtained by climate models for bare^{44,46-49} (open purple bar) and coated⁴⁴ (open red bar) BC spheres, as well as to $AAOD$ observed by the AERONET network^{44,50} (yellow bar).

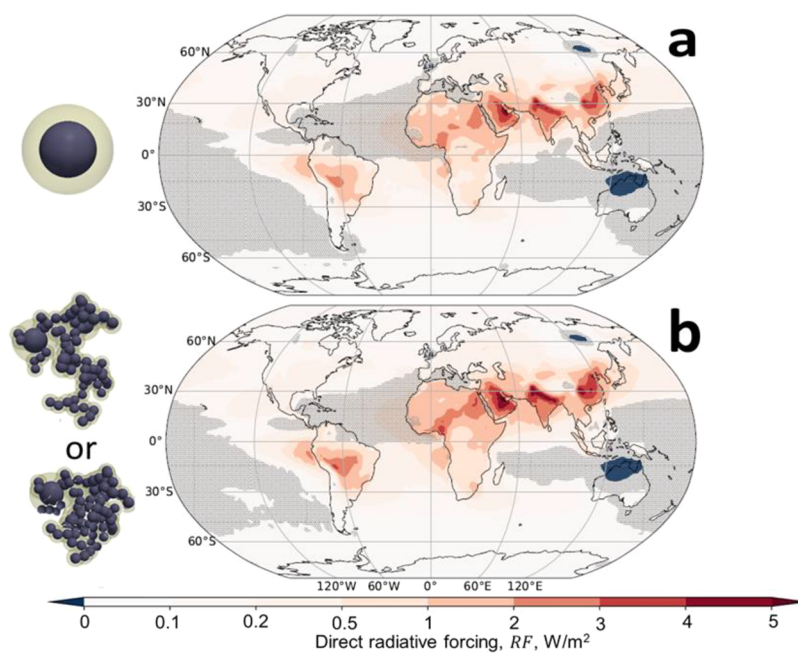


Figure 4. Global maps of the direct RF of coated spheres (a) and agglomerates (b) estimated by ECHAM-HAM. Statistically insignificant changes on the basis of interannual variability are marked by dots. Hotspots with direct $RF = 2\text{--}4\text{ W/m}^2$ assuming coated spheres (a) are seen in East, South Asia, sub-Saharan, western Africa, and the Arabian peninsula. Accounting for the realistic morphology of coated BC (b) increases its direct RF by 22% on average, in excellent agreement with the direct RF observed by AERONET in these regions.¹

about 0.1 W/m^2 . Over the hotspots of BC emissions, that is, East, South Asia, sub-Saharan, western Africa, and the Arabian peninsula, m_c/m ranges from 15 to 25. The direct RF derived here assuming coated spheres (Figure 4a) ranges between 2 and 4 W/m^2 in the above regions. Accounting for coating of BC nearly doubles the regional direct RF over that of bare BC spheres (Figure S7a), consistent with CAM3-ECA simulations.⁴⁶ However, the assumption of coated spheres still underestimates the direct $RF = 3\text{--}5\text{ W/m}^2$ of BC from field observations in these regions by 20–33% in 2005.¹ Climate models⁴⁴ used in the IPCC AR6 make similar assumptions regarding the BC morphology and thus may still underestimate the regional direct RF in 2019.

Accounting for the filamentary structure of BC increases its direct RF by 22% (on average) in the above regions (Figure S7b) compared to that of bare BC spheres (Figure S7a). The enhancement of the direct RF due to the BC agglomerate structure is slightly larger than that of MAC. This can be attributed to the $\sim 2\%$ increase of the BC absorption forcing efficiency due to the realistic BC morphology. Coating increases the direct RF of BC agglomerates by 70% in the above hotspots (Figure 4b vs Figure S7b), in excellent agreement with the observed direct RF .¹ The present ECHAM-HAM simulations do not account for nitrate and ammonium emissions.⁵² Therefore, the m_c/m derived by ECHAM-HAM was increased to elucidate the impact of BC coatings containing 46.5% and 16% of nitrates and ammonium, respectively, on BC direct RF (Figure S8) and to be consistent with the global average AAOD simulations shown in Figure 3. Accounting for nitrates and ammonium in BC coatings enhances the direct RF by about 20% (Figure S8), without affecting the agreement between ECHAM-HAM and AERONET observations.¹ Furthermore, the present ECHAM-HAM simulations for coated BC agglomerates yield an AAOD of 0.05–0.06 in the Indogangtic plains and an AAOD of

0.036–0.06 in East China (Figure S9). These AAOD values corroborate the AAOD = 0.03–0.06 observed in these regions by Gustafsson and Ramanathan⁶⁹ based on BC emissions from 2000 to 2014 and by Ramachandran and Rupakheti⁷¹ based on emissions from 2010. Most importantly, the substantial direct $RF = 3\text{--}5\text{ W/m}^2$ estimated here in these hotspots may contribute to regional climate warming by 0.75–1.25 °C. This regional temperature increase was obtained by multiplying the direct RF with a climate sensitivity of 0.25 °C/W/m^2 but without accounting for rapid adjustment effects.¹¹ Therefore, accounting for BC morphology and coating is essential to accurately estimate the large global and regional effects of BC on climate.

In conclusion, it is shown, for the first time to our knowledge, how the high observed MAC values of BC can be explained and that the climate impact of BC is dominated by its composition (i.e., RI and coating) and ramified morphology. Specifically, the enhanced light scattering between the constituent primary particles of such filamentary BC determined by the RDG theory and the resulting increased light absorption (by about 20%) agree very well with the observed absorption of BC and enhance its direct RF . Current climate models estimate the global mean AAOD of BC at 0.0014 ± 0.0006 and 0.0028 ± 0.0021 assuming bare and coated spheres, respectively. However, accounting for a realistic BC morphology and coating by weakly or non-absorbing compounds (including water), the AAOD of BC is found to be 0.0036 ± 0.0014 , in excellent agreement with satellite²⁰ and AERONET observations.^{44,50} Most importantly, ECHAM-HAM simulations accounting for the filamentary structure and coating of BC revealed large direct $RF = 3\text{--}5\text{ W/m}^2$ in East and South Asia, the sub-Saharan, western Africa, and the Arabian peninsula, explaining field observations at these regions.¹ The accurate estimation of the BC AAOD and direct RF is enabled here by accounting for a realistic BC structure

and also for its coating and *RI*. The latter is still underestimated by almost half of the climate models⁴⁴ used in the latest IPCC AR6 report. Therefore, it is essential to account for a realistic BC morphology, *RI*, and coating to make reliable estimates of the direct and indirect¹³ impact of BC on global and regional climate.

■ ASSOCIATED CONTENT

SI Supporting Information

The Supporting Information is available free of charge at <https://pubs.acs.org/doi/10.1021/acs.est.2c00428>.

Summary of coated BC properties used in recent global climate models from the IPCC AR6;⁴⁴ summary of bare BC properties used in various climate models from the IPCC AR5^{46–49} and AR6;⁴⁴ *h* of BC as a function of *d_m* for compact and open BC agglomerates of monodisperse³⁰ or polydisperse and aggregated primary particles; global map of *m_c/m* of coated BC agglomerates estimated by interfacing eq 2 with the mass concentrations of BC, sulfates, and organics derived by ECHAM-HAM; distribution of *m_c/m* and absorption forcing efficiency derived by ECHAM-HAM as a function of the altitude pressure; average volume and mass fraction of BC and coating compounds; single scattering albedo, SSA, and asymmetry factor, *g*, of coated BC as a function of its *m_c/m*; global mean direct *RF* estimated for bare and coated BC spheres, as well as bare and coated BC agglomerates along with that obtained from 2001–2009 satellite observations;²⁰ global distribution of BC direct *RF* estimated by ECHAM-HAM assuming BC (a) spheres and (b) agglomerates; global distribution of BC direct *RF* of BC (a) spheres and (b) agglomerates having coatings of constant 46.5 vol % nitrates, 16% ammonium, and varying amounts of organics and sulfates estimated by ECHAM-HAM; and global distribution of BC AAOD estimated by ECHAM-HAM for coated BC agglomerates (PDF)

■ AUTHOR INFORMATION

Corresponding Author

Georgios A. Kelesidis – Particle Technology Laboratory, Institute of Energy and Process Engineering, Department of Mechanical and Process Engineering, ETH Zürich, CH-8092 Zürich, Switzerland; orcid.org/0000-0003-4220-9649; Email: gkelesidis@ptl.mavt.ethz.ch

Authors

David Neubauer – Institute of Atmospheric and Climate Science, Department of Environmental Systems Science, ETH Zürich, CH-8092 Zürich, Switzerland

Liang-Shih Fan – Department of Chemical and Biomolecular Engineering, The Ohio State University, Columbus, Ohio 43210, United States; orcid.org/0000-0002-3892-5362

Ulrike Lohmann – Institute of Atmospheric and Climate Science, Department of Environmental Systems Science, ETH Zürich, CH-8092 Zürich, Switzerland

Sotiris E. Pratsinis – Particle Technology Laboratory, Institute of Energy and Process Engineering, Department of Mechanical and Process Engineering, ETH Zürich, CH-8092 Zürich, Switzerland

Complete contact information is available at:

<https://pubs.acs.org/10.1021/acs.est.2c00428>

Notes

The authors declare no competing financial interest.

■ ACKNOWLEDGMENTS

This research was funded by the Swiss National Science Foundation (206021_183298, 200020_182668, 250320_163243, and 206021_170729) as well as the ETH Zurich and Stavros Niarchos Foundations (ETH-08 14-2). D.N. acknowledges funding from the FORCeS project under the European Union's Horizon 2020 research program with grant agreement 821205. This work was supported by a grant from the Swiss National Supercomputing Centre (CSCS) under project ID s903. The ECHAM-HAMMOZ model is developed by a consortium composed of ETH Zurich, Max-Planck-Institut für Meteorologie, Forschungszentrum Jülich, University of Oxford, the Finnish Meteorological Institute, and the Leibniz Institute for Tropospheric Research and managed by the Center for Climate Systems Modeling (C2SM) at ETH Zurich. The authors gratefully acknowledge help from Ms. P. Crepaldi and Mr. C.A. Bruun with the DDA simulations.

■ REFERENCES

- (1) Bond, T. C.; Doherty, S. J.; Fahey, D. W.; Forster, P. M.; Berntsen, T.; DeAngelo, B. J.; Flanner, M. J.; Ghan, S.; Karcher, B.; Koch, D.; Kinne, S.; Kondo, Y.; Quinn, P. K.; Sarofim, M. C.; Schultz, M. G.; Schulz, M.; Venkataraman, C.; Zhang, H.; Zhang, S.; Bellouin, N.; Guttikunda, S. K.; Hopke, P. K.; Jacobson, M. Z.; Kaiser, J. W.; Klimont, Z.; Lohmann, U.; Schwarz, J. P.; Shindell, D.; Storelvmo, T.; Warren, S. G.; Zender, C. S. Bounding the role of black carbon in the climate system: A scientific assessment. *J. Geophys. Res.* **2013**, *118*, 5380–5552.
- (2) International Carbon Black Association, *Carbon Black User's Guide*, www.carbon-black.org, 2016, accessed on April 6, 2022.
- (3) Bond, T. C.; Bergstrom, R. W. Light absorption by carbonaceous particles: An investigative review. *Aerosol Sci. Technol.* **2006**, *40*, 27–67.
- (4) Fierce, L.; Bond, T. C.; Bauer, S. E.; Mena, F.; Riemer, N. Black carbon absorption at the global scale is affected by particle-scale diversity in composition. *Nat. Commun.* **2016**, *7*, 12361.
- (5) Solomon, S.; Plattner, G. K.; Knutti, R.; Friedlingstein, P. Irreversible climate change due to carbon dioxide emissions. *Proc. Natl. Acad. Sci. U. S. A.* **2009**, *106*, 1704–1709.
- (6) Rodhe, H.; Persson, C.; Akesson, O. An investigation into regional transport of soot and sulfate aerosols. *Atmos. Environ.* **1972**, *6*, 675–693.
- (7) Fesenfeld, L. P.; Schmidt, T. S.; Schrode, A. Climate policy for short- and long-lived pollutants. *Nat. Clim. Change* **2018**, *8*, 933–936.
- (8) Bowerman, N. H. A.; Frame, D. J.; Huntingford, C.; Lowe, J. A.; Smith, S. M.; Allen, M. R. The role of short-lived climate pollutants in meeting temperature goals. *Nat. Clim. Change* **2013**, *3*, 1021–1024.
- (9) Jacobson, M. Z. Strong radiative heating due to the mixing state of black carbon in atmospheric aerosols. *Nature* **2001**, *409*, 695–697.
- (10) Allen, M. R.; Fuglestedt, J. S.; Shine, K. P.; Reisinger, A.; Pierrehumbert, R. T.; Forster, P. M. New use of global warming potentials to compare cumulative and short-lived climate pollutants. *Nat. Clim. Change* **2016**, *6*, 773–776.
- (11) Richardson, T. B.; Forster, P. M.; Smith, C. J.; Maycock, A. C.; Wood, T.; Andrews, T.; Boucher, O.; Faluvegi, G.; Fläschner, D.; Hodnebrog, O.; Kasoar, M.; Kirkevåg, A.; Lamarque, J. F.; Mülmenstädt, J.; Myhre, G.; Olivé, D.; Portmann, R. W.; Samset, B. H.; Shawki, D.; Shindell, D.; Stier, P.; Takemura, T.; Voulgarakis, A.; Watson-Parris, D. Efficacy of Climate Forcings in PDRMIP Models. *J. Geophys. Res. Atmos.* **2019**, *124*, 12824–12844.

- (12) Skiles, S. M.; Flanner, M.; Cook, J. M.; Dumont, M.; Painter, T. H. Radiative forcing by light-absorbing particles in snow. *Nat. Clim. Change* **2018**, *8*, 964–971.
- (13) Lohmann, U.; Friebel, F.; Kanji, Z. A.; Mahrt, F.; Mensah, A. A.; Neubauer, D. Future warming exacerbated by aged-soot effect on cloud formation. *Nat. Geosci.* **2020**, *13*, 674–680.
- (14) Forster, P.; Storelvmo, T.; Armour, K.; Collins, W.; Dufresne, J. L.; Frame, D.; Lunt, D. J.; Mauritsen, T.; Palmer, M. D.; Watanabe, M.; Wild, M.; Zhang, H. The Earth's Energy Budget, Climate Feedbacks, and Climate Sensitivity. In *Climate Change 2021: The Physical Science Basis. Contribution of Working Group I to the Sixth Assessment Report of the Intergovernmental Panel on Climate Change*; Cambridge University Press: New York, 2021; In Press.
- (15) Bellouin, N.; Quaas, J.; Gryspeerdt, E.; Kinne, S.; Stier, P.; Watson-Parris, D.; Boucher, O.; Carslaw, K. S.; Christensen, M.; Daniau, A.-L.; Dufresne, J.-L.; Feingold, G.; Fiedler, S.; Forster, P.; Gettelman, A.; Haywood, J. M.; Lohmann, U.; Malavelle, F.; Mauritsen, T.; McCoy, D. T.; Myhre, G.; Mülmenstädt, J.; Neubauer, D.; Possner, A.; Rugenstein, M.; Sato, Y.; Schulz, M.; Schwartz, S. E.; Sourdeval, O.; Storelvmo, T.; Toll, V.; Winker, D.; Stevens, B. Bounding Global Aerosol Radiative Forcing of Climate Change. *Rev. Geophys.* **2020**, *58*, No. e2019RG000660.
- (16) Naik, V. S.; Szopa, S.; Adhikary, B.; Artaxo, P.; Bernsten, T.; Collins, W. D.; Fuzzi, S.; Gallardo, L.; Kiendler Scharr, A.; Klimont, Z.; Liao, H.; Unger, N.; Zanis, P. Short-Lived Climate Forcers. In *Climate Change 2021: The Physical Science Basis. Contribution of Working Group I to the Sixth Assessment Report of the Intergovernmental Panel on Climate Change*; Cambridge University Press: New York, 2021; In Press.
- (17) Kanakidou, M.; Seinfeld, J. H.; Pandis, S. N.; Barnes, I.; Dentener, F. J.; Facchini, M. C.; Van Dingenen, R.; Ervens, B.; Nenes, A.; Nielsen, C. J.; Swietlicki, E.; Putaud, J. P.; Balkanski, Y.; Fuzzi, S.; Horth, J.; Moortgat, G. K.; Winterhalter, R.; Myhre, C. E. L.; Tsigaridis, K.; Vignati, E.; Stephanou, E. G.; Wilson, J. Organic aerosol and global climate modelling: a review. *Atmos. Chem. Phys.* **2005**, *5*, 1053–1123.
- (18) Kaufman, Y. J.; Tanre, D.; Gordon, H. R.; Nakajima, T.; Lenoble, J.; Frouin, R.; Grassl, H.; Herman, B. M.; King, M. D.; Teillet, P. M. Passive remote sensing of tropospheric aerosol and atmospheric correction for the aerosol effect. *J. Geophys. Res. Atmos.* **1997**, *102*, 16815–16830.
- (19) Holben, B. N.; Tanre, D.; Smirnov, A.; Eck, T. F.; Slutsker, I.; Abuhassan, N.; Newcomb, W. W.; Schafer, J. S.; Chatenet, B.; Lavenue, F.; Kaufman, Y. J.; Castle, J. V.; Setzer, A.; Markham, B.; Clark, D.; Frouin, R.; Halthore, R.; Karneli, A.; O'Neill, N. T.; Pietras, C.; Pinker, R. T.; Voss, K.; Zibordi, G. An emerging ground-based aerosol climatology: Aerosol optical depth from AERONET. *J. Geophys. Res. Atmos.* **2001**, *106*, 12067–12097.
- (20) Chung, C. E.; Ramanathan, V.; Decremier, D. Observationally constrained estimates of carbonaceous aerosol radiative forcing. *Proc. Natl. Acad. Sci. U. S. A.* **2012**, *109*, 11624–11629.
- (21) Peng, J. F.; Hu, M.; Guo, S.; du, Z.; Zheng, J.; Shang, D. J.; Levy Zamora, M.; Zeng, L. M.; Shao, M.; Wu, Y. S.; Zheng, J.; Wang, Y.; Glen, C. R.; Collins, D. R.; Molina, M. J.; Zhang, R. Y. Markedly enhanced absorption and direct radiative forcing of black carbon under polluted urban environments. *Proc. Natl. Acad. Sci. U. S. A.* **2016**, *113*, 4266–4271.
- (22) Nelson, J. Fractality of Sooty Smoke - Implications for the Severity of Nuclear Winter. *Nature* **1989**, *339*, 611–613.
- (23) Dobbins, R. A.; Megaridis, C. M. Absorption and Scattering of Light by Polydisperse Aggregates. *Appl. Opt.* **1991**, *30*, 4747–4754.
- (24) Kelesidis, G. A.; Goudeli, E.; Pratsinis, S. E. Morphology and mobility diameter of carbonaceous aerosols during agglomeration and surface growth. *Carbon* **2017**, *121*, 527–535.
- (25) Kelesidis, G. A.; Pratsinis, S. E. Soot light absorption and refractive index during agglomeration and surface growth. *Proc. Combust. Inst.* **2019**, *37*, 1177–1184.
- (26) Kelesidis, G. A.; Pratsinis, S. E. Determination of the volume fraction of soot accounting for its composition and morphology. *Proc. Combust. Inst.* **2021**, *38*, 1189–1196.
- (27) Kelesidis, G. A.; Kholghy, M. R.; Zuercher, J.; Robertz, J.; Allemann, M.; Duric, A.; Pratsinis, S. E. Light scattering from nanoparticle agglomerates. *Powder Technol.* **2020**, *365*, 52–59.
- (28) Kelesidis, G. A.; Pratsinis, S. E. Santoro flame: The volume fraction of soot accounting for its morphology & composition. *Combust. Flame* **2022**, *240*, No. 112025.
- (29) Chakrabarty, R. K.; Heinson, W. R. Scaling Laws for Light Absorption Enhancement Due to Nonrefractory Coating of Atmospheric Black Carbon Aerosol. *Phys. Rev. Lett.* **2018**, *121*, No. 218701.
- (30) Yon, J.; Liu, F. S.; Bescond, A.; Caumont-Prim, C.; Roze, C.; Ouf, F. X.; Coppalle, A. Effects of multiple scattering on radiative properties of soot fractal aggregates. *J. Quant. Spectrosc. Radiat. Transf.* **2014**, *133*, 374–381.
- (31) Mackowski, D. W.; Mishchenko, M. I. Calculation of the T-matrix and the scattering matrix for ensembles of spheres. *J. Opt. Soc. Am. A* **1996**, *13*, 2266–2278.
- (32) Liu, F. S.; Yon, J.; Fuentes, A.; Lobo, P.; Smallwood, G. J.; Corbin, J. C. Review of recent literature on the light absorption properties of black carbon: Refractive index, mass absorption cross section, and absorption function. *Aerosol Sci. Technol.* **2019**, *54*, 33–51.
- (33) Kelesidis, G. A.; Goudeli, E.; Pratsinis, S. E. Flame synthesis of functional nanostructured materials and devices: Surface growth and aggregation. *Proc. Combust. Inst.* **2017**, *36*, 29–50.
- (34) Eggensdorfer, M. L.; Pratsinis, S. E. The Structure of Agglomerates Consisting of Polydisperse Particles. *Aerosol Sci. Technol.* **2012**, *46*, 347–353.
- (35) Moran, J.; Fuentes, A.; Liu, F.; Yon, J. FracVAL: An improved tunable algorithm of cluster-cluster aggregation for generation of fractal structures formed by polydisperse primary particles. *Comput. Phys. Commun.* **2019**, *239*, 225–237.
- (36) Spyrogianni, A.; Karadima, K. S.; Goudeli, E.; Mavrantzas, V. G.; Pratsinis, S. E. Mobility and settling rate of agglomerates of polydisperse nanoparticles. *J. Chem. Phys.* **2018**, *148*, No. 064703.
- (37) Kelesidis, G. A.; Furrer, F. M.; Wegner, K.; Pratsinis, S. E. Impact of Humidity on Silica Nanoparticle Agglomerate Morphology and Size Distribution. *Langmuir* **2018**, *34*, 8532–8541.
- (38) Leung, K. K.; Schnitzler, E. G.; Dastanpour, R.; Rogak, S. N.; Jäger, W.; Olfert, J. S. Relationship between Coating-Induced Soot Aggregate Restructuring and Primary Particle Number. *Environ. Sci. Technol.* **2017**, *51*, 8376–8383.
- (39) Draine, B. T.; Flatau, P. J. Discrete-Dipole Approximation for Scattering Calculations. *J. Opt. Soc. Am. A* **1994**, *11*, 1491–1499.
- (40) Doner, N.; Liu, F. S. Impact of morphology on the radiative properties of fractal soot aggregates. *J. Quant. Spectrosc. Radiat. Transf.* **2017**, *187*, 10–19.
- (41) Kelesidis, G. A.; Bruun, C. A.; Pratsinis, S. E. Impact of organic carbon on soot light absorption. *Carbon* **2021**, *172*, 742–749.
- (42) Saliba, G.; Subramanian, R.; Saleh, R.; Ahern, A. T.; Lipsky, E. M.; Tasoglou, A.; Sullivan, R. C.; Bhandari, J.; Mazzoleni, C.; Robinson, A. L. Optical properties of black carbon in cookstove emissions coated with secondary organic aerosols: Measurements and modeling. *Aerosol Sci. Technol.* **2016**, *50*, 1264–1276.
- (43) Liu, D. T.; Whitehead, J.; Alfara, M. R.; Reyes-Villegas, E.; Spracklen, D. V.; Reddington, C. L.; Kong, S. F.; Williams, P. L.; Ting, Y. C.; Haslett, S.; Taylor, J. W.; Flynn, M. J.; Morgan, W. T.; McFiggans, G.; Coe, H.; Allan, J. D. Black-carbon absorption enhancement in the atmosphere determined by particle mixing state. *Nat. Geosci.* **2017**, *10*, 184–188.
- (44) Sand, M.; Samset, B. H.; Myhre, G.; Gliss, J.; Bauer, S. E.; Bian, H. S.; Chin, M. A.; Checa-Garcia, R.; Ginoux, P.; Kipling, Z.; Kirkevåg, A.; Kokkola, H.; Le Sager, P.; Lund, M. T.; Matsui, H.; van Noije, T.; Olivie, D. J. L.; Remy, S.; Schulz, M.; Stier, P.; Stjern, C. W.; Takemura, T.; Tsigaridis, K.; Tsyro, S. G.; Watson-Parris, D.

Aerosol absorption in global models from AeroCom phase III. *Atmos. Chem. Phys.* **2021**, *21*, 15929–15947.

(45) Boucher, O.; Balkanski, Y.; Hodnebrog, O.; Myhre, C. L.; Myhre, G.; Quaas, J.; Samset, B. H.; Schutgens, N.; Stier, P.; Wang, R. Jury is still out on the radiative forcing by black carbon. *Proc. Natl. Acad. Sci. U. S. A.* **2016**, *113*, E5092–E5093.

(46) Kim, D.; Wang, C.; Ekman, A. M. L.; Barth, M. C.; Rasch, P. J. Distribution and direct radiative forcing of carbonaceous and sulfate aerosols in an interactive size-resolving aerosol-climate model. *J. Geophys. Res.* **2008**, *113*, D16309.

(47) Chung, S. H.; Seinfeld, J. H. Global distribution and climate forcing of carbonaceous aerosols. *J. Geophys. Res.* **2002**, *107*, 4407.

(48) Schulz, M.; Textor, C.; Kinne, S.; Balkanski, Y.; Bauer, S.; Bernsten, T.; Berglen, T.; Boucher, O.; Dentener, F.; Guibert, S.; Isaksen, I. S. A.; Iversen, T.; Koch, D.; Kirkevåg, A.; Liu, X.; Montanaro, V.; Myhre, G.; Penner, J. E.; Pitari, G.; Reddy, S.; Seland, O.; Stier, P.; Takemura, T. Radiative forcing by aerosols as derived from the AeroCom present-day and pre-industrial simulations. *Atmos. Chem. Phys.* **2006**, *6*, S225–S246.

(49) Textor, C.; Schulz, M.; Guibert, S.; Kinne, S.; Balkanski, Y.; Bauer, S.; Bernsten, T.; Berglen, T.; Boucher, O.; Chin, M.; Dentener, F.; Diehl, T.; Easter, R.; Feichter, H.; Fillmore, D.; Ghan, S.; Ginoux, P.; Gong, S.; Kristjansson, J. E.; Krol, M.; Lauer, A.; Lamarque, J. F.; Liu, X.; Montanaro, V.; Myhre, G.; Penner, J.; Pitari, G.; Reddy, S.; Seland, O.; Stier, P.; Takemura, T.; Tie, X. Analysis and quantification of the diversities of aerosol life cycles within AeroCom. *Atmos. Chem. Phys.* **2006**, *6*, 1777–1813.

(50) Chen, C.; Dubovik, O.; Henze, D. K.; Chin, M.; Lapyonok, T.; Schuster, G. L.; Ducos, F.; Fuertes, D.; Litvinov, P.; Li, L.; Lopatin, A.; Hu, Q. Y.; Torres, B. Constraining global aerosol emissions using POLDER/PARASOL satellite remote sensing observations. *Atmos. Chem. Phys.* **2019**, *19*, 14585–14606.

(51) Bevington, P. R.; Robinson, D. K. Data reduction and error analysis for the physical sciences; McGraw-Hill, 2002, pp. 36–50.

(52) Neubauer, D.; Ferrachat, S.; Siegenthaler-Le Drian, C.; Stier, P.; Partridge, D. G.; Tegen, I.; Bey, I.; Stanelle, T.; Kokkola, H.; Lohmann, U. The global aerosol-climate model ECHAM6.3-HAM2.3-Part 2: Cloud evaluation, aerosol radiative forcing, and climate sensitivity. *Geosci. Model Dev.* **2019**, *12*, 3609–3639.

(53) Myhre, G.; Samset, B. H.; Schulz, M.; Balkanski, Y.; Bauer, S.; Bernsten, T. K.; Bian, H.; Bellouin, N.; Chin, M.; Diehl, T.; Easter, R. C.; Feichter, J.; Ghan, S. J.; Hauglustaine, D.; Iversen, T.; Kinne, S.; Kirkevåg, A.; Lamarque, J.-F.; Lin, G.; Liu, X.; Lund, M. T.; Luo, G.; Ma, X.; van Noije, T.; Penner, J. E.; Rasch, P. J.; Ruiz, A.; Seland, Ø.; Skeie, R. B.; Stier, P.; Takemura, T.; Tsigaridis, K.; Wang, P.; Wang, Z.; Xu, L.; Yu, H.; Yu, F.; Yoon, J.-H.; Zhang, K.; Zhang, H.; Zhou, C. Radiative forcing of the direct aerosol effect from AeroCom Phase II simulations. *Atmos. Chem. Phys.* **2013**, *13*, 1853–1877.

(54) Zhang, K.; O'Donnell, D.; Kazil, J.; Stier, P.; Kinne, S.; Lohmann, U.; Ferrachat, S.; Croft, B.; Quaas, J.; Wan, H.; Rast, S.; Feichter, J. The global aerosol-climate model ECHAM-HAM, version 2: sensitivity to improvements in process representations. *Atmos. Chem. Phys.* **2012**, *12*, 8911–8949.

(55) Ditas, J.; Ma, N.; Zhang, Y.; Assmann, D.; Neumaier, M.; Riede, H.; Karu, E.; Williams, J.; Scharffe, D.; Wang, Q. Q.; Saturno, J.; Schwarz, J. P.; Katich, J. M.; McMeeking, G. R.; Zahn, A.; Hermann, M.; Brenninkmeijer, C. A. M.; Andreae, M. O.; Pöschl, U.; Su, H.; Cheng, Y. F. Strong impact of wildfires on the abundance and aging of black carbon in the lowermost stratosphere. *Proc. Natl. Acad. Sci. U. S. A.* **2018**, *115*, E11595–E11603.

(56) Liu, D. T.; Zhao, D. L.; Xie, Z. Z.; Yu, C. J.; Chen, Y.; Tian, P.; Ding, S.; Hu, K.; Lowe, D.; Liu, Q.; Zhou, W.; Wang, F.; Sheng, J. J.; Kong, S. F.; Hu, D. W.; Wang, Z. Z.; Huang, M. Y.; Ding, D. P. Enhanced heating rate of black carbon above the planetary boundary layer over megacities in summertime. *Environ. Res. Lett.* **2019**, *14*, 124003.

(57) Haywood, J. M.; Ramaswamy, V. Global sensitivity studies of the direct radiative forcing due to anthropogenic sulfate and black carbon aerosols. *J. Geophys. Res. Atmos.* **1998**, *103*, 6043–6058.

(58) Radney, J. G.; You, R. A.; Ma, X. F.; Conny, J. M.; Zachariah, M. R.; Hodges, J. T.; Zangmeister, C. D. Dependence of Soot Optical Properties on Particle Morphology: Measurements and Model Comparisons. *Environ. Sci. Technol.* **2014**, *48*, 3169–3176.

(59) Hallquist, M.; Wenger, J. C.; Baltensperger, U.; Rudich, Y.; Simpson, D.; Claeys, M.; Dommen, J.; Donahue, N. M.; George, C.; Goldstein, A. H.; Hamilton, J. F.; Herrmann, H.; Hoffmann, T.; Iinuma, Y.; Jang, M.; Jenkin, M. E.; Jimenez, J. L.; Kiendler-Scharr, A.; Maenhaut, W.; McFiggans, G.; Mentel, T. F.; Monod, A.; Prevot, A. S. H.; Seinfeld, J. H.; Surratt, J. D.; Szmigielski, R.; Wildt, J. The formation, properties and impact of secondary organic aerosol: current and emerging issues. *Atmos. Chem. Phys.* **2009**, *9*, S155–S236.

(60) Shamjad, P. M.; Satish, R. V.; Thamban, N. M.; Rastogi, N.; Tripathi, S. N. Absorbing Refractive Index and Direct Radiative Forcing of Atmospheric Brown Carbon over Gangetic Plain. *ACS Earth Space Chem.* **2018**, *2*, 31–37.

(61) Khalizov, A. F.; Zhang, R. Y.; Zhang, D.; Xue, H. X.; Pagels, J.; McMurry, P. H. Formation of highly hygroscopic soot aerosols upon internal mixing with sulfuric acid vapor. *J. Geophys. Res.-Atmos.* **2009**, *114*, D05208.

(62) Bellouin, N.; Rae, J.; Jones, A.; Johnson, C.; Haywood, J.; Boucher, O. Aerosol forcing in the Climate Model Intercomparison Project (CMIP5) simulations by HadGEM2-ES and the role of ammonium nitrate. *J. Geophys. Res.-Atmos.* **2011**, *116*, D20206.

(63) Wang, J. F.; Liu, D. T.; Ge, X. L.; Wu, Y. Z.; Shen, F. Z.; Chen, M. D.; Zhao, J.; Xie, C. H.; Wang, Q. Q.; Xu, W. Q.; Zhang, J.; Hu, J. L.; Allan, J.; Joshi, R.; Fu, P. Q.; Coe, H.; Sun, Y. L. Characterization of black carbon-containing fine particles in Beijing during wintertime. *Atmos. Chem. Phys.* **2019**, *19*, 447–458.

(64) Collier, S.; Williams, L. R.; Onasch, T. B.; Cappa, C. D.; Zhang, X. L.; Russell, L. M.; Chen, C. L.; Sanchez, K. J.; Worsnop, D. R.; Zhang, Q. Influence of Emissions and Aqueous Processing on Particles Containing Black Carbon in a Polluted Urban Environment: Insights From a Soot Particle-Aerosol Mass Spectrometer. *J. Geophys. Res.-Atmos.* **2018**, *123*, 6648–6666.

(65) McMeeking, G. R.; Morgan, W. T.; Flynn, M.; Highwood, E. J.; Turnbull, K.; Haywood, J.; Coe, H. Black carbon aerosol mixing state, organic aerosols and aerosol optical properties over the United Kingdom. *Atmos. Chem. Phys.* **2011**, *11*, 9037–9052.

(66) Gong, X. D.; Zhang, C.; Chen, H.; Nizkorodov, S. A.; Chen, J. M.; Yang, X. Size distribution and mixing state of black carbon particles during a heavy air pollution episode in Shanghai. *Atmos. Chem. Phys.* **2016**, *16*, 5399–5411.

(67) Hu, K.; Zhao, D. L.; Liu, D. T.; Ding, S.; Tian, P.; Yu, C. J.; Zhou, W.; Huang, M. Y.; Ding, D. P. Estimating radiative impacts of black carbon associated with mixing state in the lower atmosphere over the northern North China Plain. *Chemosphere* **2020**, *252*, No. 1226455.

(68) Wang, Y. Y.; Liu, F. S.; He, C. L.; Bi, L.; Cheng, T. H.; Wang, Z. L.; Zhang, H.; Zhang, X. Y.; Shi, Z. B.; Li, W. J. Fractal Dimensions and Mixing Structures of Soot Particles during Atmospheric Processing. *Environ. Sci. Technol. Lett.* **2017**, *4*, 487–493.

(69) Gustafsson, O.; Ramanathan, V. Convergence on climate warming by black carbon aerosols. *Proc. Natl. Acad. Sci. U. S. A.* **2016**, *113*, 4243–4245.

(70) Ramanathan, V.; Carmichael, G. Global and regional climate changes due to black carbon. *Nat. Geosci.* **2008**, *1*, 221–227.

(71) Ramachandran, S.; Rupakheti, M. Inter-annual and seasonal variations in columnar aerosol characteristics and radiative effects over the Pokhara Valley in the Himalayan foothills - Composition, radiative forcing, and atmospheric heating. *Environ. Pollut.* **2020**, *264*, No. 114799.